



**AFRL-RX-WP-TP-2011-4372**

**MICROSTRUCTURE AND PROPERTIES OF A  
REFRACTORY NbCrMo0.5Ta0.5ZrTi ALLOY (PREPRINT)**

**C.F. Woodward**

**Metals Branch**

**Metals, Ceramics & Nondestructive Evaluation Division**

**O.N. Senkov**

**UES, Inc.**

**OCTOBER 2011**

**Approved for public release; distribution unlimited.**

*See additional restrictions described on inside pages*

**STINFO COPY**

**AIR FORCE RESEARCH LABORATORY  
MATERIALS AND MANUFACTURING DIRECTORATE  
WRIGHT-PATTERSON AIR FORCE BASE, OH 45433-7750  
AIR FORCE MATERIEL COMMAND  
UNITED STATES AIR FORCE**

REPORT DOCUMENTATION PAGE					Form Approved OMB No. 0704-0188	
<p>The public reporting burden for this collection of information is estimated to average 1 hour per response, including the time for reviewing instructions, searching existing data sources, gathering and maintaining the data needed, and completing and reviewing the collection of information. Send comments regarding this burden estimate or any other aspect of this collection of information, including suggestions for reducing this burden, to Department of Defense, Washington Headquarters Services, Directorate for Information Operations and Reports (0704-0188), 1215 Jefferson Davis Highway, Suite 1204, Arlington, VA 22202-4302. Respondents should be aware that notwithstanding any other provision of law, no person shall be subject to any penalty for failing to comply with a collection of information if it does not display a currently valid OMB control number. <b>PLEASE DO NOT RETURN YOUR FORM TO THE ABOVE ADDRESS.</b></p>						
1. REPORT DATE (DD-MM-YY) October 2011		2. REPORT TYPE Technical Paper		3. DATES COVERED (From - To) 1 October 2011 – 1 October 2011		
4. TITLE AND SUBTITLE MICROSTRUCTURE AND PROPERTIES OF A REFRACTORY NbCrMo0.5Ta0.5ZrTi ALLOY (PREPRINT)				5a. CONTRACT NUMBER In-house		
				5b. GRANT NUMBER		
				5c. PROGRAM ELEMENT NUMBER 62102F		
6. AUTHOR(S) C.F. Woodward (Metals Branch/Metals, Ceramics & Nondestructive Evaluation Division) O.N. Senkov(UES, Inc.)				5d. PROJECT NUMBER 4347		
				5e. TASK NUMBER 20		
				5f. WORK UNIT NUMBER LM121100		
7. PERFORMING ORGANIZATION NAME(S) AND ADDRESS(ES) Metals Branch/Metals, Ceramics & Nondestructive Evaluation Division Air Force Research Laboratory, Materials and Manufacturing Directorate Wright-Patterson Air Force Base, OH 45433-7750 Air Force Materiel Command, United States Air Force				8. PERFORMING ORGANIZATION REPORT NUMBER AFRL-RX-WP-TP-2011-4372		
9. SPONSORING/MONITORING AGENCY NAME(S) AND ADDRESS(ES) Air Force Research Laboratory Materials and Manufacturing Directorate Wright-Patterson Air Force Base, OH 45433-7750 Air Force Materiel Command United States Air Force				10. SPONSORING/MONITORING AGENCY ACRONYM(S) AFRL/RXLM		
				11. SPONSORING/MONITORING AGENCY REPORT NUMBER(S) AFRL-RX-WP-TP-2011-4372		
12. DISTRIBUTION/AVAILABILITY STATEMENT Approved for public release; distribution unlimited.						
13. SUPPLEMENTARY NOTES The U.S. Government is joint author of this work and has the right to use, modify, reproduce, release, perform, display or disclose the work. PA Case Number and clearance date: 88ABW-2011-3436, 14 Jun 2011. Preprint journal article to be submitted to Acta Materialia. This document contains color.						
14. ABSTRACT A new refractory alloy, Nb <sub>20</sub> Cr <sub>20</sub> Mo <sub>10</sub> Ta <sub>10</sub> Zr <sub>20</sub> Ti <sub>20</sub> , was produced by vacuum arc melting. To close shrinkage porosity, it was hot isostatically pressed (HIPd) at T = 1723 K and P = 207 MPa for 3 hours. In both as-solidified and HIPd conditions, the alloy contained three phases: two body centered cubic (BCC1 and BCC2) and one face centered cubic (FCC). The BCC1 phase was slightly enriched with Nb, Mo and Ta and depleted with Zr and Cr, and its lattice parameter after HIP was a = 324.76 ± 0.16 pm. The BCC2 phase was enriched with Zr and Ti and considerably depleted with Mo, Cr and Ta, and its lattice parameter after HIP was estimated to be a = 341.0 ± 1.0 pm. The FCC phase was highly enriched with Cr and it was identified as a Laves C15 phase, (Zr,Ta)(Cr,Mo,Nb) <sub>2</sub> , with the lattice parameter a = 733.38 ± 0.18 pm. The volume fractions of the BCC1, BCC2 and FCC phases were 68.5%, 9.6% and 21.9%, respectively. The alloy density and Vickers microhardness were ρ = 8.23 ± 0.01 g/cm <sup>3</sup> and Hv = 5288 ± 71 MPa.						
15. SUBJECT TERMS alloy design; high entropy alloy; crystallography; microstructure; mechanical properties						
16. SECURITY CLASSIFICATION OF:			17. LIMITATION OF ABSTRACT: SAR	NUMBER OF PAGES 28	19a. NAME OF RESPONSIBLE PERSON (Monitor) Andrew Rosenberger	
a. REPORT Unclassified	b. ABSTRACT Unclassified	c. THIS PAGE Unclassified			19b. TELEPHONE NUMBER (Include Area Code) N/A	

# MICROSTRUCTURE AND PROPERTIES OF A REFRACTORY NbCrMo<sub>0.5</sub>Ta<sub>0.5</sub>ZrTi ALLOY

O.N. Senkov<sup>1,2,\*</sup> and C.F. Woodward<sup>1</sup>

<sup>1</sup> Air Force Research Laboratory, Materials and Manufacturing Directorate, Wright-Patterson Air Force Base, OH 45433, USA

<sup>2</sup> UES, Inc., Dayton, OH 45432, USA

## ABSTRACT

A new refractory alloy, Nb<sub>20</sub>Cr<sub>20</sub>Mo<sub>10</sub>Ta<sub>10</sub>Zr<sub>20</sub>Ti<sub>20</sub>, was produced by vacuum arc melting. To close shrinkage porosity, it was hot isostatically pressed (HIPd) at  $T = 1723$  K and  $P = 207$  MPa for 3 hours. In both as-solidified and HIPd conditions, the alloy contained three phases: two body centered cubic (BCC1 and BCC2) and one face centered cubic (FCC). The BCC1 phase was slightly enriched with Nb, Mo and Ta and depleted with Zr and Cr, and its lattice parameter after HIP was  $a = 324.76 \pm 0.16$  pm. The BCC2 phase was enriched with Zr and Ti and considerably depleted with Mo, Cr and Ta, and its lattice parameter after HIP was estimated to be  $a = 341.0 \pm 1.0$  pm. The FCC phase was highly enriched with Cr and it was identified as a Laves C15 phase, (Zr,Ta)(Cr,Mo,Nb)<sub>2</sub>, with the lattice parameter  $a = 733.38 \pm 0.18$  pm. The volume fractions of the BCC1, BCC2 and FCC phases were 68.5%, 9.6% and 21.9%, respectively. The alloy density and Vickers microhardness were  $\rho = 8.23 \pm 0.01$  g/cm<sup>3</sup> and  $H_v = 5288 \pm 71$  MPa. The alloy had compression yield strength of 1595 MPa at 296 K, 983 MPa at 1073 K, 546 MPa at 1273 K and 171 MPa at 1473 K. During deformation at 296 K and 1073 K, the alloy showed ductile fracture after plastic compression strain of ~5-6%. No macroscopic fracture was observed after 50% compression strain at 1273 K and 1473 K.

**Keywords:** Alloy design; high entropy alloy; crystallography; microstructure; mechanical properties.

\* Corresponding author. Phone: 937-2551320, e-mail: oleg.senkov@wpafb.af.mil

# 1 INTRODUCTION

Metallic alloys with superior mechanical properties at elevated temperatures and low density remain in high demand for the aerospace industry. For example, the specific core power of a high pressure turbine engine is known to increase with an increase in the turbine rotor inlet temperature and significant turbine engine efficiencies can be achieved by running at higher temperatures [1]. These applications have benefited from decades of development of nickel-based (Ni) superalloys, which have allowed a steady increase in operating temperatures and led to improved performance and efficiency [2]. Currently, Ni-based superalloys have the best combination of required elevated temperature properties, such as creep resistance, temperature capability, environmental resistance, and damage tolerance, among all other known alloys. However, operating temperatures are reaching the theoretical limits of these materials, whose incipient melting temperatures are in the range of 1440-1540 K, depending on the composition. Engineering solutions to this materials problem requires active or passive cooling thus increasing parasitic weight and decreasing overall flight efficiency and capability (maneuverability, fuel consumption, etc.) of supersonic/hypersonic vehicles. New metallic materials with higher melting points, such as refractory molybdenum (Mo) and niobium (Nb) alloys, are now being seriously examined as alternatives by academic and industrial groups [3,4,5].

The refractory metals and alloys, a group of metallic materials with melting points above 2123 K, are creep resistant at temperatures above 1073 K. High temperature strength and creep resistance are the key properties of these alloys, since considerable alloy softening generally occurs at temperatures above  $\sim 0.5-0.6T_m$ , where  $T_m$  is the absolute melting temperature. At the same time, poor low-temperature ductility, poor oxidation resistance at high temperatures and high density limit the range of applications of many refractory alloys. In recent publications [6,7,8,9] a new, so called high entropy alloying (HEA) approach initially invented by Yeh et al. [10,11,12], was used to develop new refractory alloys, which contain several principal alloying elements at near equiatomic concentrations. These are  $\text{Ta}_{25}\text{Nb}_{25}\text{W}_{25}\text{Mo}_{25}$ ,  $\text{Ta}_{20}\text{Nb}_{20}\text{W}_{20}\text{Mo}_{20}\text{V}_{20}$  [6,7] and  $\text{Ta}_{20}\text{Nb}_{20}\text{Hf}_{20}\text{Zr}_{20}\text{Ti}_{20}$  [8,9]. All three alloys had a single-phase BCC crystal structure. The two alloys containing W, retained extremely high strength at temperatures at least up to 1873 K; however, they were brittle at room temperature. At the same time, the  $\text{Ta}_{20}\text{Nb}_{20}\text{Hf}_{20}\text{Zr}_{20}\text{Ti}_{20}$  alloy showed high strength and very good ductility at room temperature [8], however, the strength of this alloy rapidly decreased to below 100 MPa at temperatures

above 1473 K and cavitation occurred during deformation at  $T \sim 1073$  K and strain rates above  $10^{-3} \text{ s}^{-1}$  [9]. Among these three alloys, the  $\text{Ta}_{20}\text{Nb}_{20}\text{Hf}_{20}\text{Zr}_{20}\text{Ti}_{20}$  alloy had the lowest density of  $9.8 \text{ g/cm}^3$ .

This paper reports on a new refractory alloy,  $\text{Nb}_{20}\text{Cr}_{20}\text{Mo}_{10}\text{Ta}_{10}\text{Zr}_{20}\text{Ti}_{20}$ . By replacing Hf and half of Ta with lighter Cr and Mo, respectively, the density of this alloy was reduced to  $8.2 \text{ g/cm}^3$ . In addition, the new alloy showed improved high temperature strength, relative to the  $\text{Ta}_{20}\text{Nb}_{20}\text{Hf}_{20}\text{Zr}_{20}\text{Ti}_{20}$  alloy, and improved room temperature ductility, relative to the  $\text{Ta}_{25}\text{Nb}_{25}\text{W}_{25}\text{Mo}_{25}$ ,  $\text{Ta}_{20}\text{Nb}_{20}\text{W}_{20}\text{Mo}_{20}\text{V}_{20}$  alloys.

## 2 EXPERIMENTAL PROCEDURES

The  $\text{Nb}_{20}\text{Cr}_{20}\text{Mo}_{10}\text{Ta}_{10}\text{Zr}_{20}\text{Ti}_{20}$  alloy was prepared by vacuum arc melting of the pure elements. Nb, Cr Ti and Zr were taken at equal molar fractions, while the molar fractions of Mo and Ta were twice smaller. Titanium and zirconium were in the form of 3.175 mm diameter slugs with purities of 99.98% and 99.95%, respectively. Niobium, tantalum and molybdenum were in the form of 1.0, 2.0 and 4.6 mm diameter rods, and their purities were 99.95%, 99.9% and 99.0%, respectively. Chromium was in the form of 3 to 12 mm pieces with the purity of 99.95%. High vacuum of  $2.1 \times 10^{-4} \text{ N/m}^2$  was achieved in the arc melting chamber prior to filling the chamber with high purity argon at the pressure of  $5.1 \times 10^4 \text{ N/m}^2$ . High purity molten titanium was used as a getter for residual oxygen, nitrogen and hydrogen. Arc melting of the alloy was conducted on a water-cooled copper plate. To achieve homogeneous distribution of elements, the alloy was re-melted and flipped five times, and was in a liquid state for about 5 minutes during each melting event. The prepared sample was about 15 mm thick, 35 mm wide and 100 mm long and had shiny surfaces. The actual alloy composition determined with the use of inductively-coupled plasma-optical emission spectroscopy (ICP-OES), is given in Table 1. The crystal structure was identified with the use of a Rigaku X-ray diffractometer,  $\text{Cu K}\alpha$  radiation, and the  $2\theta$  range of  $5^\circ$  to  $140^\circ$ .

To close porosity in the as-solidified alloy, it was hot isostatically pressed (HIPd) under the following conditions. The alloy sample was placed inside a 63 mm diameter alumina can. The alumina can was inserted inside a 75 mm diameter graphite can, which was used as a heating element and located inside the HIP unit chamber. The chamber was evacuated to  $\sim 1.3 \times 10^{-4} \text{ N/m}^2$ , filled with high purity argon and the sample was heated at a constant rate of  $10 \text{ K/min}$  to

1723 K with a simultaneous increase in the argon pressure in the chamber to 207 MN/m<sup>2</sup>. The sample was held at 1723 K / 207 MN/m<sup>2</sup> for 3 hour and cooled to room temperature at 20 K/min with simultaneous pressure release.

The density of the alloy was measured with an AccuPyc 1330 V1.03 pycnometer. The pycnometer cell volume was 12.2284 cm<sup>3</sup>, the weight of the sample was ~10 g and was measured with the accuracy of  $\pm 0.0001$  g, and the volume of the samples was determined with the accuracy of  $\pm 0.0001$  cm<sup>3</sup> by measuring the free volume of the loaded cell using helium gas and ten purges. Vickers microhardness was measured on polished cross-section surfaces using a 136-degree Vickers diamond pyramid under 500 g load applied for 30 seconds. The microstructure was analyzed with the use of a scanning electron microscope (SEM) equipped with a backscatter electron (BSE), energy-dispersive X-ray spectroscopy (EDS), and electron backscatter diffraction (EBSD) detectors. A step size of 0.2  $\mu$ m was used for simultaneous EDS and EBSD mapping.

Cuboids-shaped specimens for compression testing were electric-discharge machined from the HIPd alloy. The specimen compression axis was perpendicular to the alloy surface, which was in contact with the copper plate during arc melting. The specimen surfaces were mechanically polished and the compression faces of the specimens were paralleled and lubricated with boron nitride (for elevated temperature tests). The specimen's dimensions were 4.7 mm x 4.7 mm x 7.7 mm. Compression tests were conducted at temperatures 1073 K, 1273 K and 1473 K in a computer-controlled Instron (Instron, Norwood, MA) mechanical testing machine outfitted with a Brew vacuum furnace and silicon carbide dies. Prior to each test, the furnace chamber was evacuated to  $\sim 10^{-4}$  N/m<sup>2</sup>. The test specimen was then heated to the test temperature at a heating rate of  $\sim 20$  K/min and soaked at the temperature for 15 minutes under 5 N controlled load, and then compressed to a 50% height reduction or to fracture, whichever happened first. A constant ramp speed that corresponded to an initial strain rate of  $10^{-3}$  s<sup>-1</sup> was used. Room temperature testing was conducted at the same loading conditions but in air, and a thin Teflon foil was used between the compression faces and silicon carbide dies to reduce friction. The deformation of all specimens was video-recorded and an optical setup was used to measure strain versus load.

### 3 RESULTS AND DISCUSSION

#### 3.1 Crystal Structure and Microstructure

Figure 1 shows the X-ray diffraction patterns of the NbCrMo<sub>0.5</sub>Ta<sub>0.5</sub>TiZr alloy in (a) as-solidified and (b) HIP'd conditions. The diffraction peaks from three phases, two with the body-centered cubic (BCC1 and BCC2) lattices and one with the face centered cubic (FCC, Laves C15) lattice, are easily identified in the as-solidified condition (see Figure 1a). The lattice parameters of the BCC1, BCC2 and FCC phases were determined to be  $a = 325.46 \pm 0.11$  pm,  $338.6 \pm 0.4$  pm, and  $733.38 \pm 0.18$  pm, respectively. The HIP processing broadened the X-ray peaks from the BCC1 and FCC phases and reduced the intensities of the peaks of the BCC2 and FCC phases relative to the peak intensities of the BCC1 phase (Figure 1b). The lattice parameter of the BCC1 phase slightly decreased ( $a = 324.76 \pm 0.16$  pm), BCC2 phase increased ( $a = 341 \pm 1$  pm) and FCC phase increased ( $a = 740.0 \pm 0.5$  pm) after HIP.

Microstructure of the HIPd alloy is shown in Figure 2. Three characteristic constituents are clearly recognized on the backscatter electron (BSE) images. These are (i) large branching bright particles, (ii) a dark continuous matrix between the bright particles, and (iii) smaller dark particles precipitated inside the matrix. The electron backscatter diffraction (EBSD) analysis indicated that both the bright particles and the dark matrix have the BCC crystal structures, while the smaller dark particles have a FCC crystal structure (Figure 3a, b). Note that in the secondary electron (SE) image mode, Figure 3a, the light-gray color code of the FCC particles is similar to the color code of large BCC1 particles. Although the EBSD method cannot distinguish the BCC1 and BCC2 phases, which have different lattice parameters, these phases can be identified by comparing their volume fractions. Indeed, the volume fractions of the light particles, dark particles and the matrix were determined to be ~67%, 17% and 16%, respectively. Comparing these results with the results of X-ray diffraction, one may conclude that the light particles have the BCC1 crystal structure, while the matrix phase has the BCC2 crystal structure. EDS mapping showed that these phases have different concentrations of alloying elements. For example, Figure 3c illustrates that the concentration of Ti is much higher in the BCC2 phase than in the BCC1 phase, while the FCC phase has the lowest concentration of Ti.

Quantitative chemical analysis of these three phases was conducted with the use of an EDS detector attached to the field emission gun SEM. The results are given in Table 2. It is found that

the BCC1 phase is slightly enriched with Nb, Mo and Ta, which are the BCC forming elements, and depleted with Cr and Zr. The amount of Ti in the BCC1 phase is close to the average alloy composition. The BCC2 phase, on the other hand, is highly enriched with Ti and Zr and depleted with Cr, Mo and Ta. The amount of Nb in this phase is only slightly lower of the average alloy composition. In spite of the reduced amount of the BCC-forming elements in the BCC2 phase, their total concentration is still high, ~26 at.%, to stabilize the high-temperature polymorph of the Ti and Zr rich phase. Finally, the FCC phase contains an increased amount of Cr (~41 at.%) and reduced amounts of Mo, Nb, Ta and Ti. This Laves phase can be described by a formula (Zr,Ta)(Cr, Mo, Nb)<sub>2</sub>, with Ti equally substituting both larger and smaller elements.

It is interesting to note that the inverse pole figure (IPF) maps from the BCC and FCC phases, Figure 3 (d-f), show that the BCC2 matrix grains have the same crystallographic orientations as the adjacent BCC1 particles. On the other hand, no correlation between the crystallographic orientations of the BCC2 matrix and FCC particles was identified. This result may indicate that the BCC1 and BCC2 phases originated from the same high-temperature single BCC phase.

During cooling, Cr-enriched FCC particles randomly precipitated along grain boundaries of this high-temperature BCC phase thus changing the composition of the adjacent areas and leading to formation of the BCC2 phase with a considerably reduced amount of Cr, Mo and Ta. According to this suggested scenario, the BCC1 should be considered as the high-temperature matrix phase and BCC2 phase as a secondary phase formed as a result of a solid-state phase transformation.

Additional work is required for studying solid state reactions in this alloy.

Using the rule of mixtures (i.e. Vegard's law [13]) and known concentrations of the alloying elements in the BCC1 and BCC2 phases, one can calculate the crystal lattice parameter  $a_{\text{mix}}$  of the respective disordered BCC solid solutions:

$$a_{\text{mix}} = \sum c_i a_i \quad (1)$$

Here  $c_i$  is the atomic fraction of element  $i$  and  $a_i$  is the lattice parameter of the BCC crystal lattice of element  $i$  at room temperature. The calculated (Calc)  $a_{\text{mix}}$  are given in Table 3 along with the experimental (Exp)  $a$  values determined from the X-ray diffraction. The calculated and experimental values of  $a$  for the BCC1 phase are practically the same; however, the experimental value of  $a$  for the BCC2 phase in the HIPd alloy is about 0.5% higher than the respective



calculated value. This discrepancy can be due to a large experimental error in determining  $a$  from low-intensity X-ray diffraction peaks of the BCC2 phase. The same calculated and experimental values of the lattice parameter suggest that the alloying elements are randomly distributed in the BCC phases.

### 3.2 Density and Micro-Hardness

The density of the alloy in the as-solidified and HIPd conditions was determined to be  $\rho = 8.02 \pm 0.01 \text{ g/cm}^3$  and  $8.23 \pm 0.01 \text{ g/cm}^3$ , respectively. A 2.6% increase in the alloy density after HIPing is probably due to closing porosity, which is eventually present in the as-solidified material.

Using the densities of pure elements (Table 4) and the alloy composition (Table 1), one can estimate the density,  $\rho_{mix}$ , of a disordered solid solution of the same composition using the rule of mixtures:

$$\rho_{mix} = \frac{\sum c_i A_i}{\sum \frac{c_i A_i}{\rho_i}} \quad (2)$$

Here  $A_i$  and  $\rho_i$  are the atomic weight and density of element  $i$ . Thus calculated  $\rho_{mix}$  value is  $8.23 \text{ g/cm}^3$ , which is exactly the same as the density of HIPd alloy. The fact that the average alloy density follows the rule of mixtures of pure elements, in spite of the alloy contains 2 disordered BCC phases with the total volume fraction of 83% and one ordered FCC phase with the volume fraction of 17%, may indicate that the decomposition of the high-temperature single BCC phase into these three phases did not affect the average coefficient of thermal expansion and, thus, density of the alloy at room temperature.

Vickers microhardness  $H_v$  of the HIPd alloy was measured in twenty randomly selected locations and the average value was 5288 MPa. The scatter around the average microhardness value was  $\Delta H_v = \pm 71 \text{ MPa}$ . The microhardness of the alloy does not follow the rule of mixtures of the respective properties of the constituent elements. Indeed, Table 5 shows typical  $H_v$  [14] values for pure elements at room temperature. Using the rule of mixtures, the microhardness,  $(H_v)_{mix} = \sum c_i H_{vi}$ , was calculated to be  $(H_v)_{mix} = 1097 \text{ MPa}$ . This value is much smaller than the experimental  $H_v$  value. The high microhardness of the alloy is likely originated from the combination of precipitation and solid solution-like strengthening.

### 3.3 Compression Properties and Microstructure of Deformed Alloy

#### 3.3.1 Compression properties

The engineering stress,  $\sigma$ , vs. engineering strain,  $\varepsilon$  curves of the NbCrMo<sub>0.5</sub>Ta<sub>0.5</sub>TiZr alloy obtained during compression testing at different temperatures are shown in Figure 4. The yield strength values,  $\sigma_{0.2}$ , at  $\varepsilon_p = 0.2\%$ , where  $\varepsilon_p$  is the engineering plastic strain, peak strength,  $\sigma_p$ , and fracture strain are given in Table 6. During deformation at 296 K, the yield strength was 1595 MPa and continuous strengthening occurred until the alloy fractured by localized shear at the peak strength of 2046 MPa accumulating about 5% strain. During testing at  $T = 1073$  K,  $\sigma_{0.2}$  decreased to 983 MPa, the peak strength of 1100 MPa was achieved at 4.2% strain and the sample fractured by shear at about 5.5-6% strain, after a decrease in strength to 1050 MPa. An increase in the testing temperature to 1273 K resulted in a considerable softening of the alloy after a short stage of strain hardening. At this temperature,  $\sigma_{0.2} = 546$  MPa,  $\sigma_p = 630$  MPa and the minimum strength achieved during strain softening was 393 MPa after about 22% plastic strain. At this temperature, the sample did not fracture. An increase in the temperature to 1473 K, led to further decrease in the flow stress of the alloy and  $\sigma_{0.2}$  was 170 MPa. The peak stress of 190 MPa was reached shortly after yielding and followed by weak softening and a steady state flow at  $\sigma_{min} = 135$  MPa. No sample fracture occurred at this temperature.

#### 3.4.2 Microstructure of deformed samples

Typical microstructure features of the fracture surface of the alloy sample deformed at room temperature are shown in Figure 5. A mixture of ductile and brittle fracture can be seen at low magnification in Figure 5a. The ductile fracture leads to formation of dimples of different sizes and morphology Figure 5(b-d), while the brittle fracture occurs by quazi-cleavage of the FCC (Laves) phase, as well as along the interfaces Figure 5(a,d).

The brittle nature of the Laves phase also led to low ductility at 1073 K. Fracture at this temperature occurred along the boundaries between the BCC2 and Laves phases, Figure 6(a-d); however, few cracks propagated inside the large BCC1 particles can also be seen in Figure 6a and Figure 6b. Fine (secondary) BCC1 particles precipitated near the original (primary) large BCC1 particles inside the BCC2 phase are seen in Figure 6d. Their size rapidly decreases with an increase in the distance from the primary BCC1 particle, which the small particles are

associated with. It is likely that the solubility of Nb, Mo and Ta in the BCC2 phase is considerably higher at 1073 K than at room temperature and the heavy elements start to diffuse from the primary BCC1 particle into the adjacent BCC2 matrix leading to partial dissolution of the BCC1 phase. The concentration of Nb, Mo and Ta is thus the highest near the primary particle interface and exponentially decreases with an increase in the distance from the interface. Upon cooling after testing, re-precipitation of the BCC1 phase occurs. Due to a strong temperature dependence of the solubility, the precipitation in the regions with higher concentration of the elements occurs at higher temperatures. This leads to formation of larger secondary particles near the primary BCC1 particles and smaller particles at larger distances. Knowing the width of the region,  $l$ , where the precipitation occurred ( $l \sim 6 \mu\text{m}$ ) and the time of the specimen holding at 1073 K ( $t \sim 1800 \text{ s}$ ) the effective diffusion coefficient,  $D_{\text{eff}}$ , of these elements in the BCC2 phase during compression at 1073 K can be estimated as  $D_{\text{eff}} = l^2/(2t) \approx 10^{-8} \text{ cm}^2/\text{s}$ . This estimated value is about 3 orders of magnitude higher than the reported diffusion coefficient of Nb at the same temperature in BCC Zr-Nb alloys [15] and more than 8 orders of magnitude higher than the reported self-diffusion coefficient of Nb [16]. However, the diffusivity of elements is known to considerably increase during plastic deformation [17].

A representative microstructure of the HIPd alloy after 50% compression at 1273 K is shown in Figure 7. The primary BCC1 particles are compressed in the loading direction, Figure 7a. No cracks or porosity are detected. Fine equiaxed secondary BCC1 particles precipitate inside the BCC2 matrix near the surfaces of large BCC1 particles, similar to the situation observed in a sample deformed at 1073 K. However, these fine particles are coarser after deformation at 1273 K (compare Figure 7c and Figure 6d) and their average size is estimated to be  $\sim 0.7\text{-}0.8 \mu\text{m}$ . In addition, many of these particles in Figure 7a are aligned in chains oriented about 60-70 degrees to the compression direction and form characteristic tails at the respective primary particles. These aligned chains of fine particle are likely associated with the direction of the local shear propagation. A round primary BCC1 particle sheared at about 40 degrees to the compression direction is also seen in Figure 7a, and it is shown in Figure 7c at a higher magnification. On the opposite sides of this particle there are two tails of fine particles, which are oriented in the same,  $\sim 40$ -degree direction. These observations indicate that the local plastic flow changes orientation in the deformed alloy sample within  $\sim 100 \mu\text{m}$  scale. They also indicate that the fine secondary BCC1 particles or were already present in the alloy during deformation, or the regions of the

BCC2 matrix, which were adjacent to the large BCC1 particles and enriched with Nb, Mo and Ta were heavily deformed and moved away from the particle interfaces at 1273 K, but the fine particles were formed inside these regions during cooling due to the temperature-dependent solubility. Additional work is required to identify the correct scenario of formation of the aligned chains of fine BCC1 particles. Fine, nanometer-size precipitates of the Laves phase are observed inside the primary BCC1 particles, Figure 7d. These precipitates are coarser at grain boundaries and accompany with the formation of fine particles of the BCC2 phase, Figure 7d. To separate two effects, temperature and deformation, on the microstructure evolution, the microstructure of an un-loaded sample, which was heated to 1273 K, held at this temperature and cooled down to room temperature identically to the deformed sample, was studied. The microstructure of this sample is given in Figure 8. Contrary to the deformed sample, precipitation of fine secondary BCC1 particles around the primary particles is not well developed and the number density and the size of these particles are much smaller in the un-deformed sample (compare Figure 8b with Figure 7b and Figure 8c with Figure 7c). Instead of the fine secondary particles, the primary particles in the un-deformed sample are surrounded by  $\sim 2\text{-}3\text{ }\mu\text{m}$  thick transition layers that likely have the element content which is intermediate between the compositions of the BCC1 and BCC2 phases. Precipitation of nanometer-size Laves phase particles is observed inside the primary BCC1 particles; however, almost all these particles precipitate at grain/subgrain boundaries and they are much finer than similar particles in the deformed sample. This comparison of the microstructure of the deformed and un-deformed sample supports our suggestion that the deformation accelerates diffusion-related processes, such as phase transformations and particle coarsening.

Figure 9 illustrates a microstructure of the HIPd alloy after 50% compression at 1473 K. Many primary BCC1 particles become elongated and some are severely deformed in the directions of plastic flow of the material, Figure 9a. Similar to deformation at 1273 K, these particles have characteristic tails oriented in the directions of local plastic flow (see Figure 9a and Figure 9b). However, while at 1273 K these tails consist of fine separated secondary BCC1 particles embedded in the BCC2 phase, at 1473 K the tails consist of joined, larger size ( $\sim 2\text{-}3\text{ }\mu\text{m}$ ) particles (see Figure 9c). Deformation of the BCC2 matrix results in recrystallization and formation of equiaxed grains, Figure 9d. At the same time, the FCC (Laves) particles embedded in the BCC2 matrix remain practically non-deformed. Twins, observed inside these particles, are

probably annealing twins as they are also observed in non-deformed samples. Fine precipitates observed inside the primary BCC1 particles become clearly visible due to coarsening. These precipitates decorate grain boundaries, but they are also present inside the grains (see Figure 9b). The EBSD analysis indicates that these precipitates are the Laves phase with the FCC crystal structure (Figure 10).

#### **4 CONCLUSIONS**

A new refractory alloy,  $\text{NbCrMo}_{0.5}\text{Ta}_{0.5}\text{Ti}_{20}\text{Zr}_{20}$ , was produced and its crystal structure, microstructure, density, hardness and compression properties were determined in the as-solidified and HIPd condition. The alloy consisted of two disordered BCC1 and BCC2 phases and one ordered FCC (Laves C15) phase. After HIP at 1723 K, 207 MPa for 3 hours, the BCC1 phase was present in the form of large individual particles, which were surrounded by the BCC2 phase. Smaller particles of the Laves phase were present inside the BCC2 phase. The volume fractions of the BCC1, BCC2 and FCC phases were 67%, 16% and 17%, respectively. The HIPd alloy density was  $\rho = 8.23 \text{ g/cm}^3$  and the Vickers microhardness was  $H_v = 5.29 \text{ GPa}$ . The alloy showed high yield strengths of  $\sigma_{0.2} = 1595 \text{ MPa}$ , 983 MPa, 546 MPa, and 170 MPa at 293 K, 1073 K, 1273 K and 1473 K, respectively. Ductile type fracture occurred after  $\sim 5\text{-}6\%$  compression strain at 293 K and 1073 K. Brittle Laves particles were responsible for the fracture at these temperatures. No fracture occurred during compression testing at 1273 K and 1473 K.

#### **ACKNOWLEDGEMENTS**

Discussions with Drs. D. Miracle, D. Dimiduk, B. Viswanathan, and G. Wilks are recognized. Technical help from J.M. Scott (mechanical testing) and S. Senkova (SEM) is acknowledged. This work was supported through the Air Force Office of Scientific Research (Dr. Ali Sayir, Program Manager) and through the USAF Contract No. FA8650-10-D-5226.

## TABLES

Table 1. Chemical composition of the NbCrMo<sub>0.5</sub>Ta<sub>0.5</sub>TiZr alloy produced by vacuum arc melting.

Composition	Nb	Cr	Mo	Ta	Ti	Zr
At. %	21.84	18.39	10.04	11.86	19.40	18.48
Wt. %	23.30	10.98	11.06	24.64	10.67	19.36

Table 2. Chemical composition (in at.%) of the BCC1, BCC2 and FCC phases in the HIPd NbCrMo<sub>0.5</sub>Ta<sub>0.5</sub>TiZr alloy.

Phase\Element	Nb	Cr	Mo	Ta	Ti	Zr
BCC1	26.80	13.22	14.30	16.80	19.07	9.82
BCC2	18.68	3.09	0.64	3.83	33.16	40.60
FCC	12.07	40.74	6.35	6.99	10.78	23.09

Table 3. The lattice parameter,  $a$ , of the BCC crystal structure of the pure metals and the BCC1 and BCC2 phases presented in the studied alloy at room temperature. For Zr and Ti, the parameter  $a$  was extrapolated from elevated temperatures [8]. The calculated (Calc) values of the lattice parameter for the alloy were obtained using Equation 1.

Metal	Nb	Cr	Mo	Ta	Ti	Zr	BCC1 Calc	BCC2 Calc	BCC1 HIP	BCC2 HIP
$a$ , pm	330.1	288.4	315.0	330.3	327.6	358.2	324.7	339.3	324.8	341.0

Table 4. Density of pure metals and the studied NbCrMo<sub>0.5</sub>Ta<sub>0.5</sub>TiZr alloy. Both calculated (Calc, using Eq. 3) and experimental (Exp) values are shown for the alloy

Metal	Nb	Cr	Mo	Ta	Ti	Zr	Alloy Calc	Alloy Cast	Alloy HIP
$\rho$ , g/cm <sup>3</sup>	8.57	7.14	10.28	16.65	4.51	6.51	8.23	8.02	8.23

Table 5. Vickers microhardness,  $H_v$ , values of pure metals and the NbCrMo<sub>0.5</sub>Ta<sub>0.5</sub>TiZr alloy at room temperature. Both the calculated (Calc, Equation 2) and experimental (Exp) values are shown for the alloy.

Metal	Nb	Cr	Mo	Ta	Ti	Zr	Alloy Calc	Alloy Exp
$H_v$ , MPa	1320	1060	1530	873	970	903	1097	5288

Table 6. Compression yield strength,  $\sigma_{0.2}$ , peak stress,  $\sigma_p$ , and fracture strain of the NbCrMo<sub>0.5</sub>Ta<sub>0.5</sub>TiZr alloy at different temperatures. The strain rate is  $10^{-3} \text{ s}^{-1}$ .

T, K	296	1073	1273	1473
$\sigma_{0.2}$ , MPa	1595	983	546	170
$\sigma_p$ , MPa	2046	1100	630	190
$\varepsilon_f$ , %	5.0	5.5	No fracture	No fracture

## FIGURE CAPTIONS

Figure 1. X-ray diffraction pattern of the NbCrMo<sub>0.5</sub>Ta<sub>0.5</sub>TiZr alloy in (a) as-solidified and (b) HIPd conditions. The indexed peaks belong to two BCC and one FCC crystal phases.\

Figure 2. SEM backscatter electron images of a polished cross-section of the HIPd NbCrMo<sub>0.5</sub>Ta<sub>0.5</sub>TiZr alloy. The three phases with different morphologies and contrasts are indicated.

Figure 3. (a) Secondary electron (SE) image, (b) phase map, (c) EDS map of Ti, and (d,e) inverse pole figure (IPF) maps of (d) the BCC and (e) FCC phases. In (b), the BCC phases are colored by red and the FCC phase is colored by green. In figure (c), the lighter regions are enriched and darker regions are depleted with Ti. The crystallographic orientations of different grains in figures (d) and (e) are identified by the color scheme in the IPF triangle (f).

Figure 4. The engineering stress versus engineering strain compression curves of HIPd NbCrMo<sub>0.5</sub>Ta<sub>0.5</sub>TiZr alloy samples at 296 K, 1073 K, 1273 K, and 1473 K.

Figure 5. SEM secondary electron images of the fracture surface of an NbCrMo<sub>0.5</sub>Ta<sub>0.5</sub>TiZr alloy samples after compression deformation at room temperature.

Figure 6. SEM backscatter images of the microstructure of an NbCrMo<sub>0.5</sub>Ta<sub>0.5</sub>TiZr alloy sample after compression deformation at 1073 K.

Figure 7. SEM backscatter images of the microstructure of an NbCrMo<sub>0.5</sub>Ta<sub>0.5</sub>TiZr alloy sample after compression deformation at 1273 K. The compression direction is vertical.

Figure 8. SEM backscatter images of the microstructure of an NbCrMo<sub>0.5</sub>Ta<sub>0.5</sub>TiZr alloy sample after holding at 1273 K for 1460 seconds. This sample experienced the same heating and cooling conditions as the sample compressed at 1273 K.

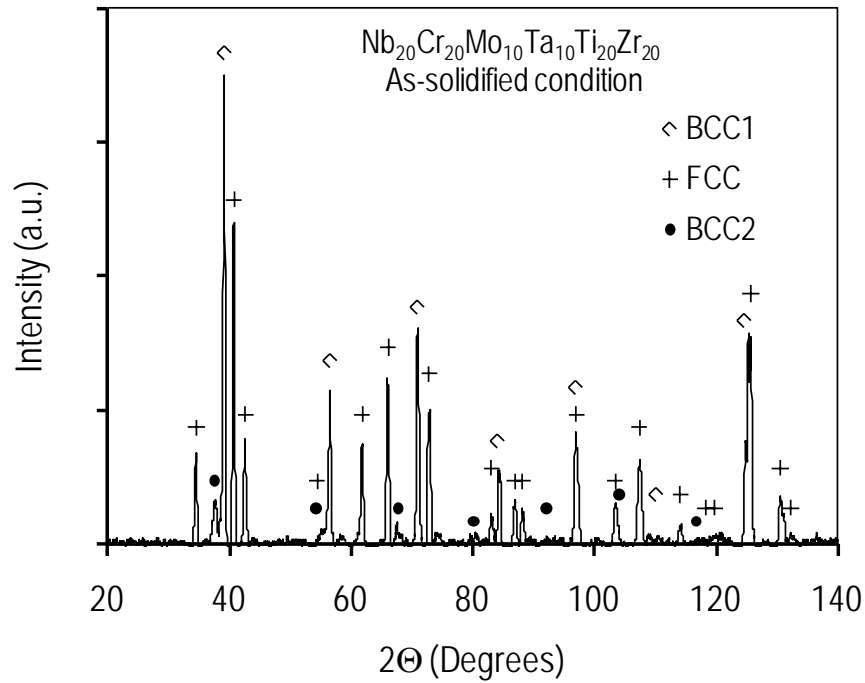


Figure 9. SEM backscatter images of the microstructure of an NbCrMo<sub>0.5</sub>Ta<sub>0.5</sub>TiZr alloy sample after compression deformation at 1473 K. The compression direction is vertical.

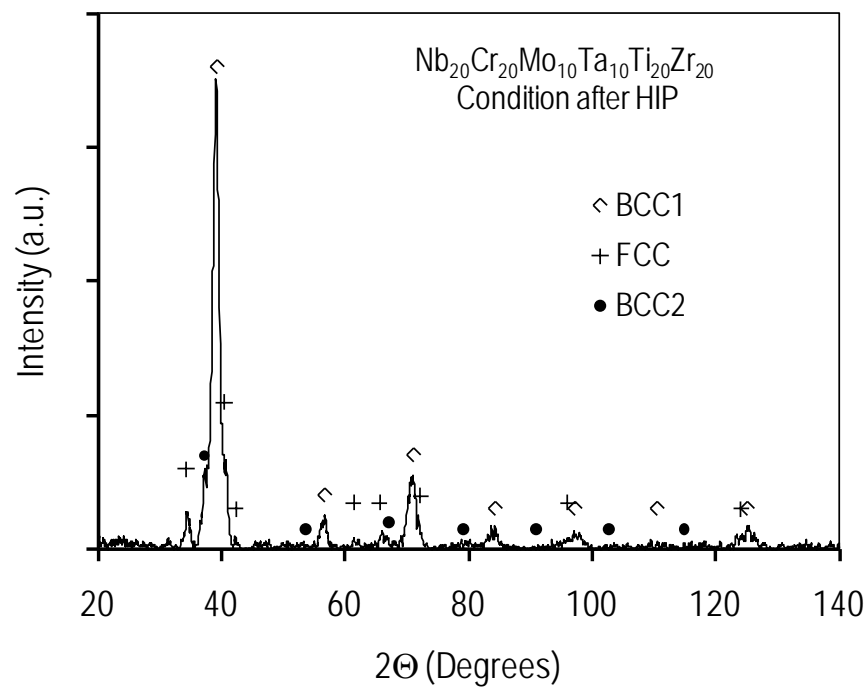
Figure 10. (a) SEM secondary electron image of the microstructure of an NbCrMo<sub>0.5</sub>Ta<sub>0.5</sub>TiZr alloy sample after compression at 1473 K and (b) respective phase map. The BCC phases are red and the FCC (Laves) phase is green.

## REFERENCES

- 1 D.M. Dimiduk and J.H. Perepezko, MRS Bulletin, 28 (2003) 639-645.
- 2 R.A. MacKay, T.P. Gabb, J.L. Smialek, and M.V. Nathal, Alloy Design Challenge: Development of Low Density Superalloys for Turbine Blade Applications, NASA/TM—2009-215819.
- 3 P.R. Subramanian, M.G. Mendiratta, D.M. Dimiduk, M.A. Stucke, Mater. Sci. Eng. A2390240 (1997) 1-13.
- 4 B.P. Bewlay, M.R. Jackson, J.-C. Zhao, and P.R. Subramanian, Metall. Mater. Trans. A 34A (2003) 2043-2052.
- 5 J.H. Perepezko, Science, 326, No. 5956 (2009) 1068-1069.
- 6 O.N. Senkov, G.B. Wilks, D.B. Miracle, C.P. Chuang, P.K. Liaw, Intermetallics, 18 (2010) 1758-1765.
- 7 O.N. Senkov, G.B. Wilks, J.M. Scott, D.B. Miracle, Intermetallics, 2011 (in press).
- 8 O.N. Senkov, J.M. Scott, S.V. Senkova, D.B. Miracle, C.F. Woodward, J. Alloys Comp. 509 (2011) 6043-6048.
- 9 O.N. Senkov, J.M. Scott, S.V. Senkova, D.B. Miracle, C.F. Woodward, Acta Mater. (submitted in February 2011)
- 10 J.-W. Yeh, S.-K. Chen, S.-J. Lin, J.-Y. Gan, T.-S. Chin, T.-T. Shun, C.-H. Tsau, S.-Y. Chang, Adv. Eng. Mater. 6 (5) (2004) 299–303.
- 11 J.-W. Yeh, Annales de Chimie: Science des Materiaux, 31 (2006) 633-648.
- 12 J.-W. Yeh, Y.-L. Chen, S.-J. Lin, S.-K. Chen, Mater. Sci. Forum, 560 (2007) 1-9.
- 13 L. Vegard, Zeitschrift fur Physik, 5 (1021) 17-26.
- 14 Hardnesses of the elements:  
[http://en.wikipedia.org/wiki/Hardnesses\\_of\\_the\\_elements\\_\(data\\_page\)](http://en.wikipedia.org/wiki/Hardnesses_of_the_elements_(data_page))
- 15 Chr. Herzig, U. Kohler and S.V. Divinski, J. Appl. Phys. 85 (1999) 8119-8130.
- 16 R.E. Einziger, J.N. Mundy, H.A. Hoff, Phys. Rev. B 17 (1978) 440-448.
- 17 O.N. Senkov, M.M. Myshlyaev, Acta Metall. 34 (1986) 97-106.



(a)



(b)

Figure 1. X-ray diffraction patterns of the  $\text{NbCrMo}_{0.5}\text{Ta}_{0.5}\text{TiZr}$  alloy in (a) as-solidified and (b) HIPd conditions. The indexed peaks belong to two BCC and one FCC crystal phases.

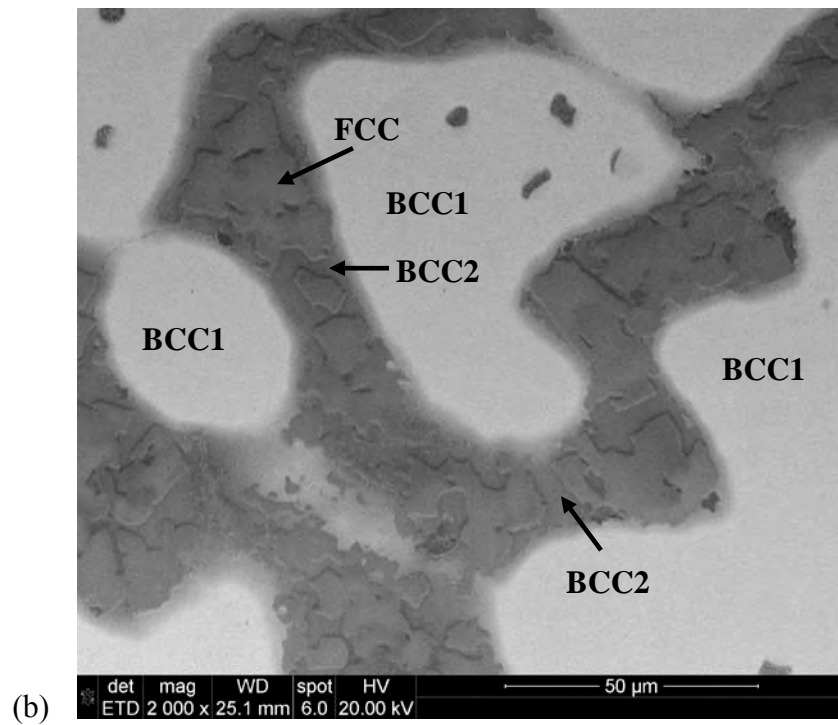
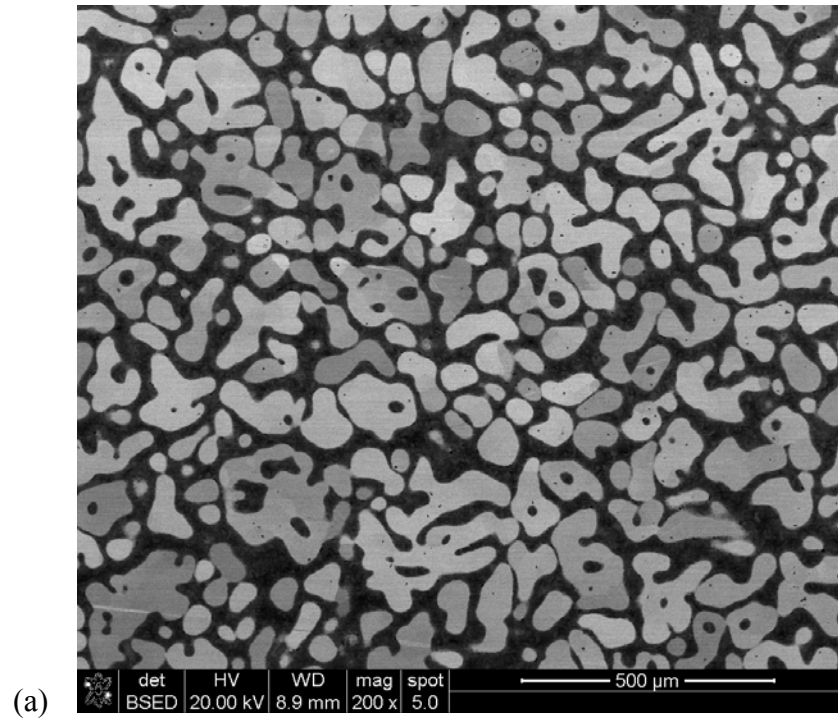


Figure 2. SEM backscatter electron images of a polished cross-section of the HIPd NbCrMo<sub>0.5</sub>Ta<sub>0.5</sub>TiZr alloy. The three phases with different morphologies and contrasts are indicated.

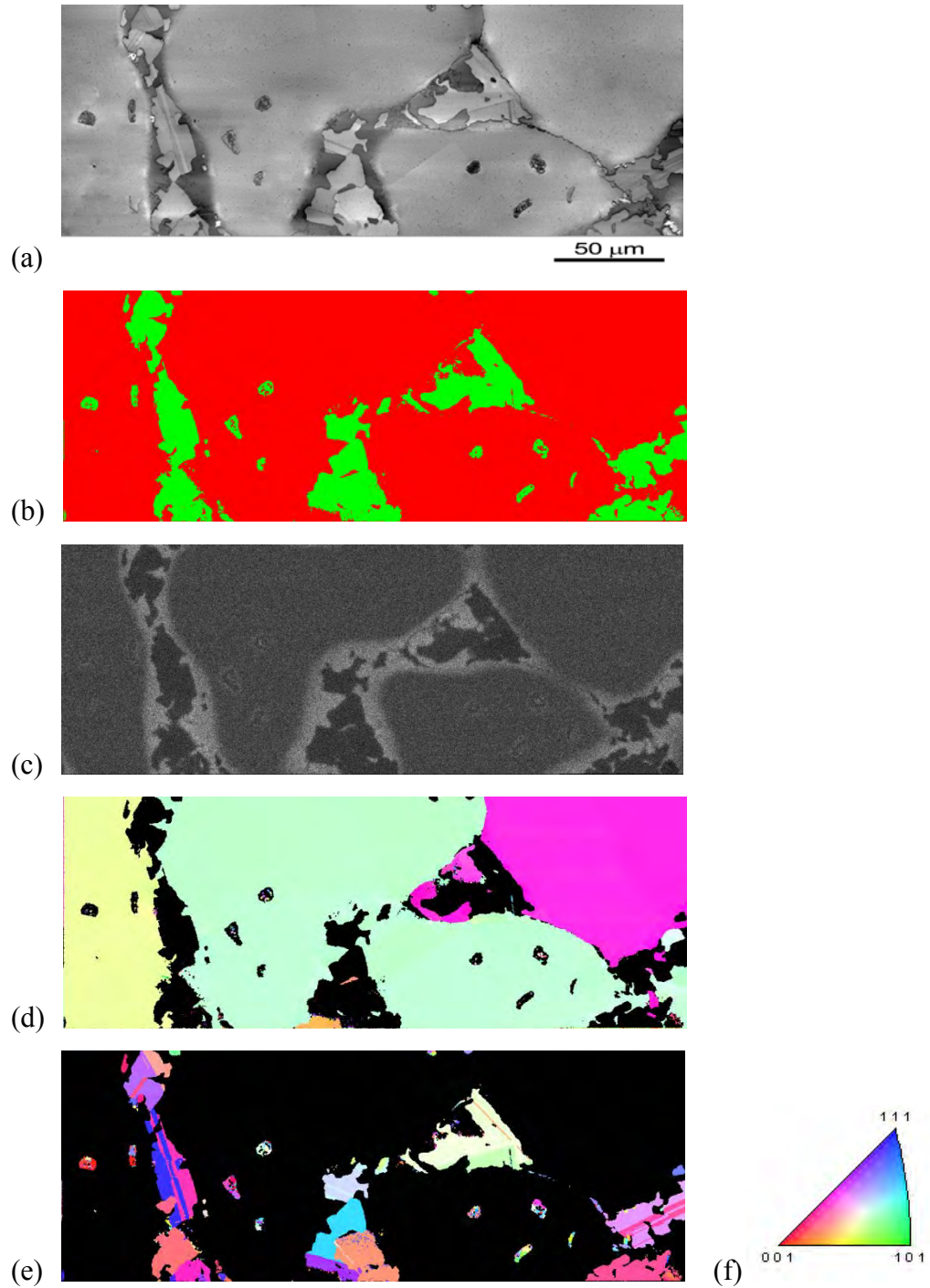


Figure 3. (a) Secondary electron (SE) image, (b) phase map, (c) EDS map of Ti, and (d,e) inverse pole figure (IPF) maps of (d) the BCC and (e) FCC phases. In (b), the BCC phases are colored by red and the FCC phase is colored by green. In figure (c), the lighter regions are enriched and darker regions are depleted with Ti. The crystallographic orientations of different grains in figures (d) and (e) are identified by the color scheme in the IPF triangle (f).

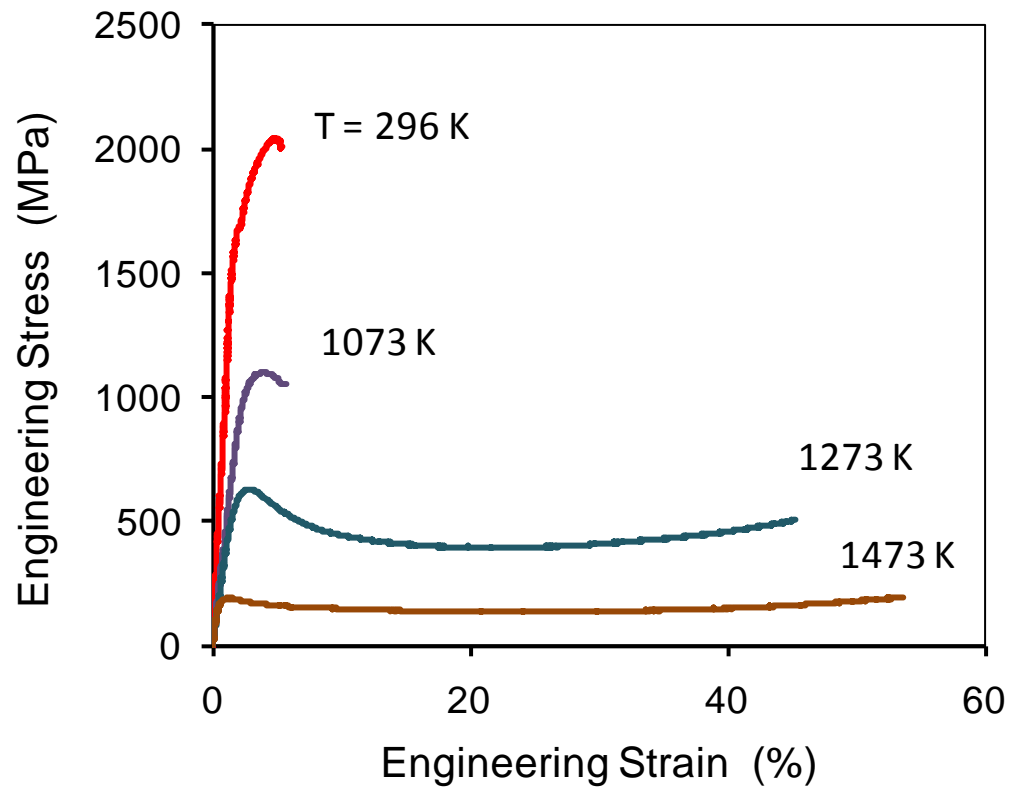


Figure 4. The engineering stress versus engineering strain compression curves of HIPd NbCrMo<sub>0.5</sub>Ta<sub>0.5</sub>TiZr alloy samples at 296 K, 1073 K, 1273 K, and 1473 K.

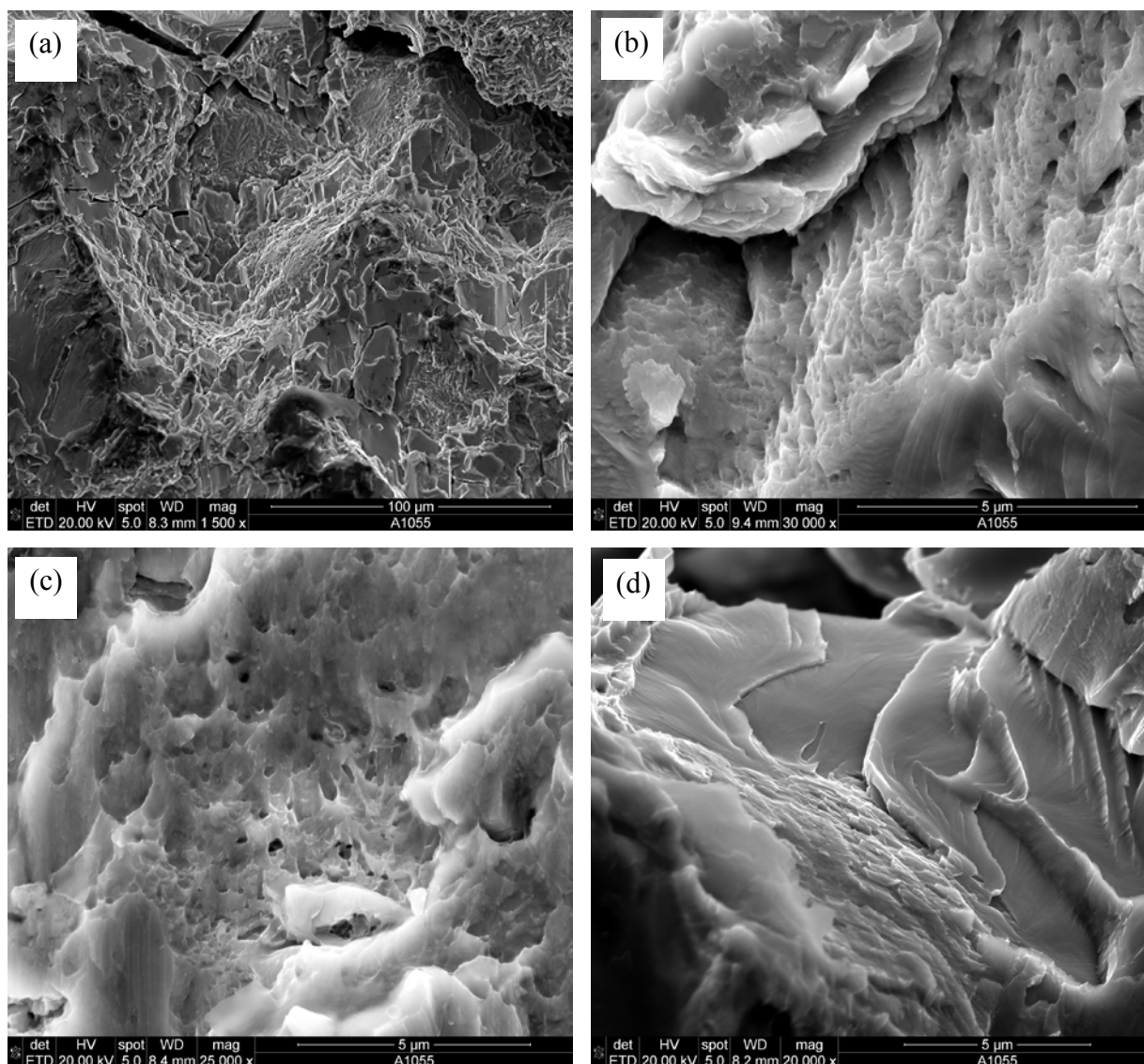


Figure 5. SEM secondary electron images of the fracture surface of an NbCrMo<sub>0.5</sub>Ta<sub>0.5</sub>TiZr alloy samples after compression deformation at room temperature.

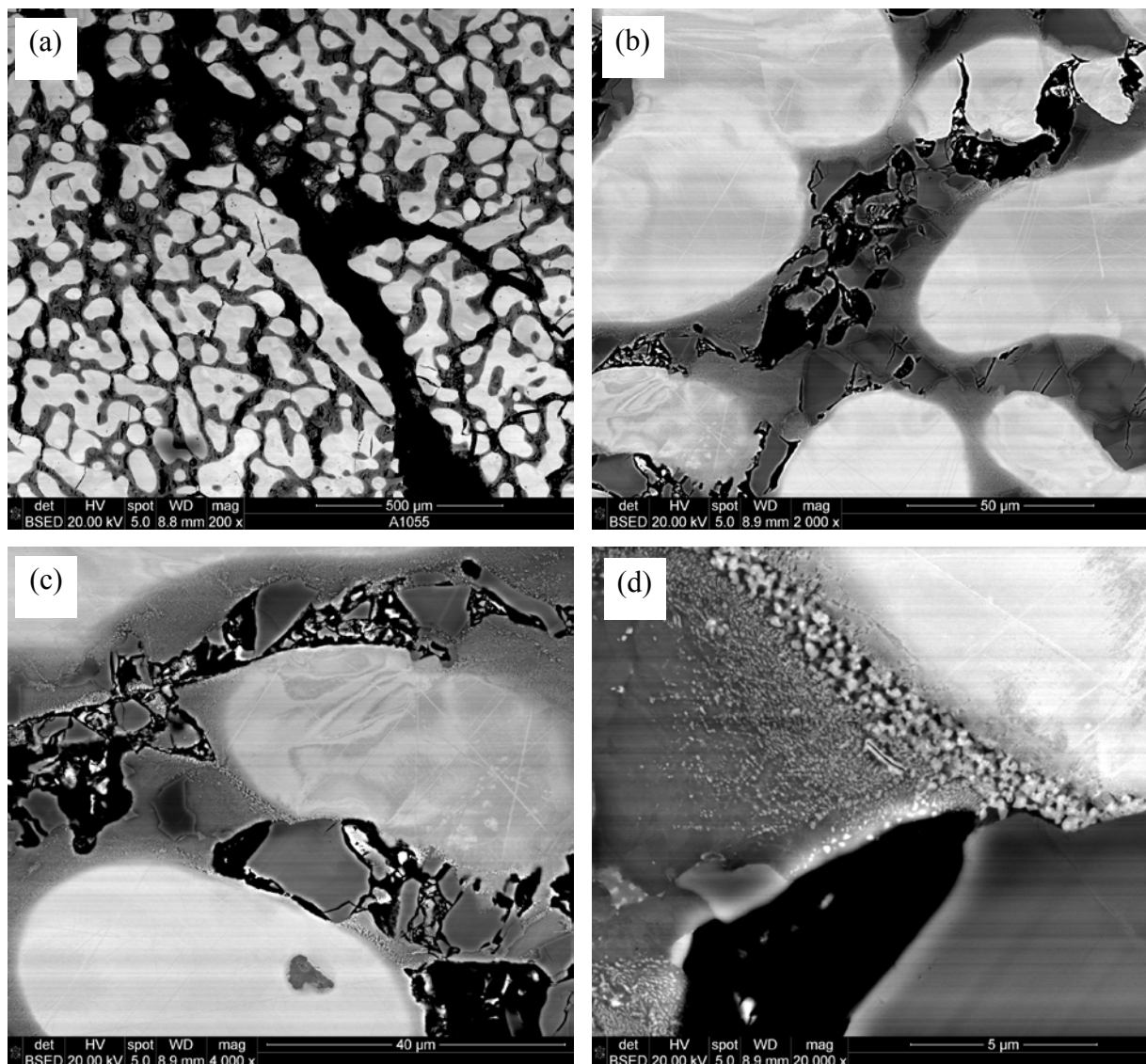


Figure 6. SEM backscatter images of the microstructure of an NbCrMo<sub>0.5</sub>Ta<sub>0.5</sub>TiZr alloy sample after compression deformation at 1073 K. The compression direction is vertical.



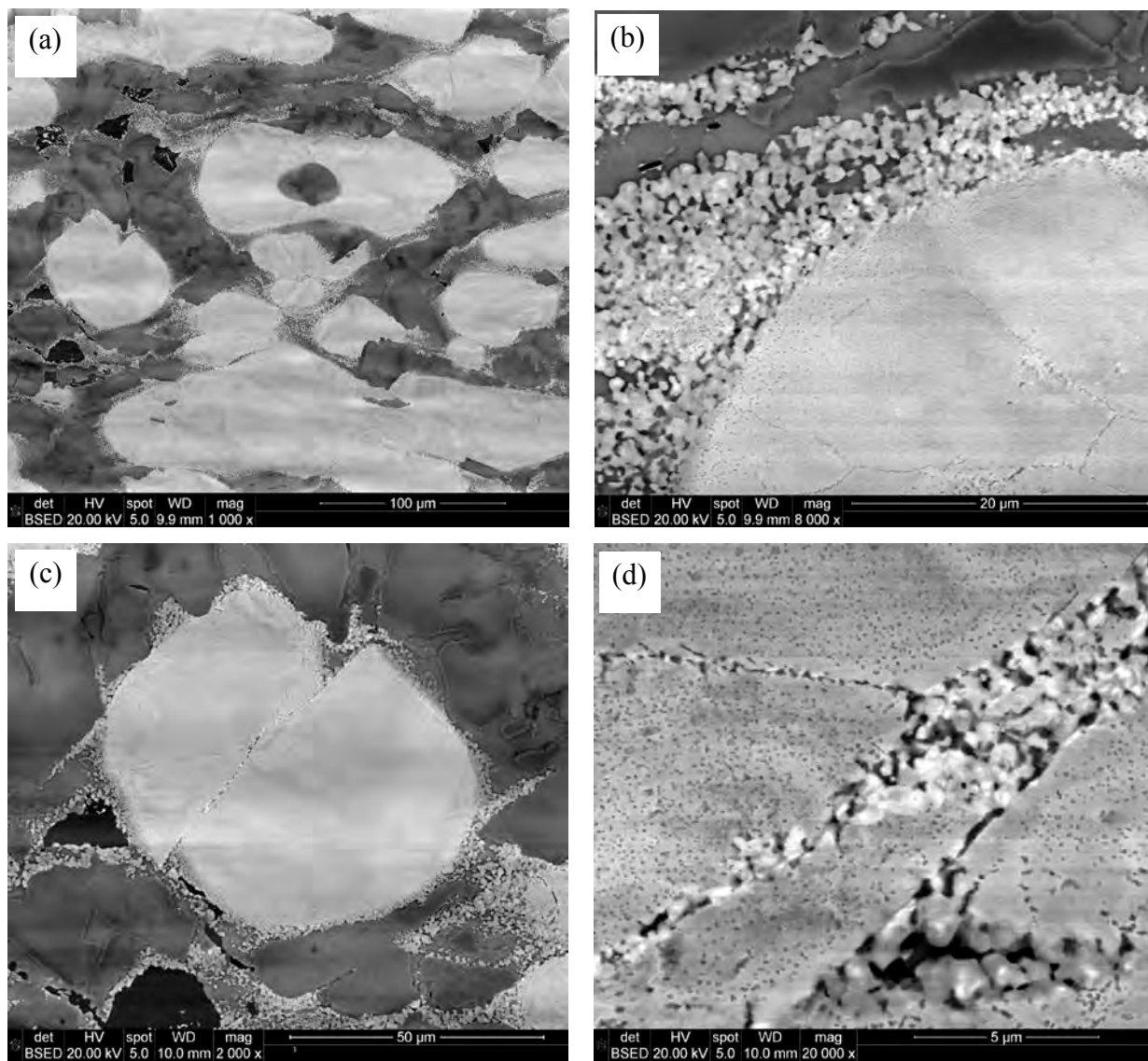


Figure 7. SEM backscatter images of the microstructure of an NbCrMo<sub>0.5</sub>Ta<sub>0.5</sub>TiZr alloy sample after compression deformation at 1273 K. The compression direction is vertical.

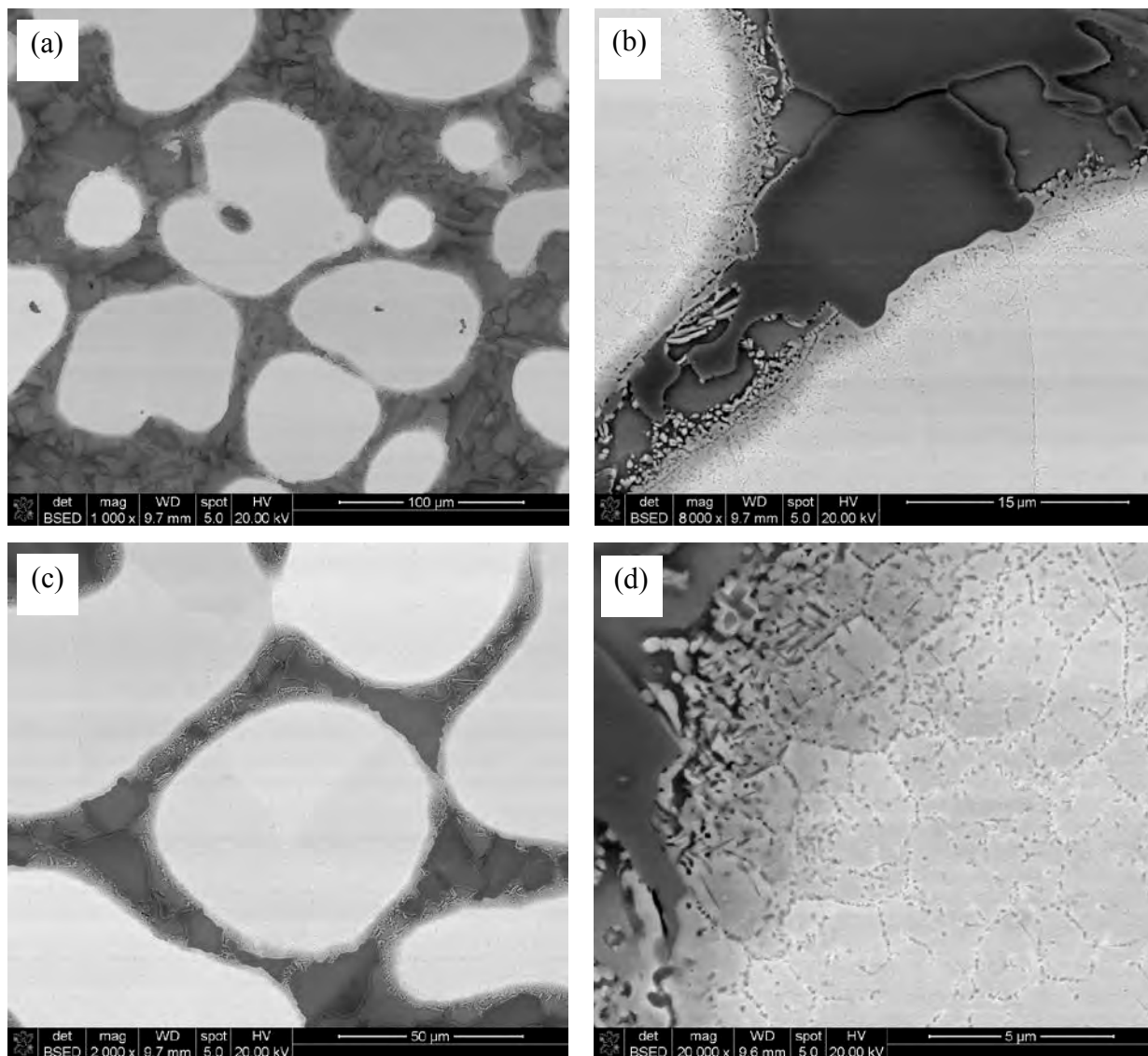


Figure 8. SEM backscatter images of the microstructure of an NbCrMo<sub>0.5</sub>Ta<sub>0.5</sub>TiZr alloy sample after holding at 1273 K for 1460 seconds. This sample experienced the same heating and cooling conditions as the sample compressed at 1273 K (see Figure 7). The figures are arranged by their magnifications similar to Figure 7.

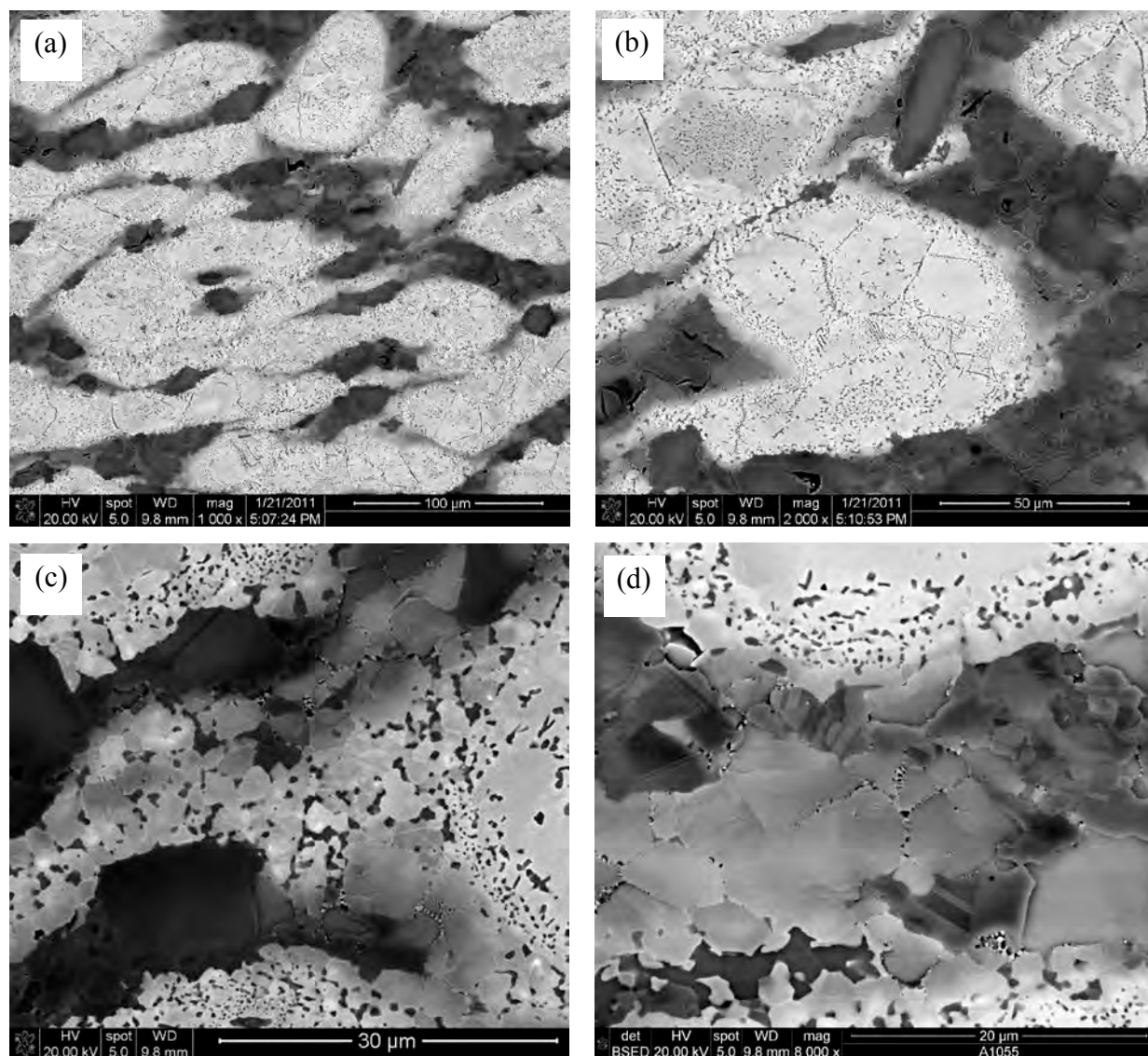


Figure 9. SEM backscatter images of the microstructure of an NbCrMo<sub>0.5</sub>Ta<sub>0.5</sub>TiZr alloy sample after compression deformation at 1473 K. The compression direction is vertical.

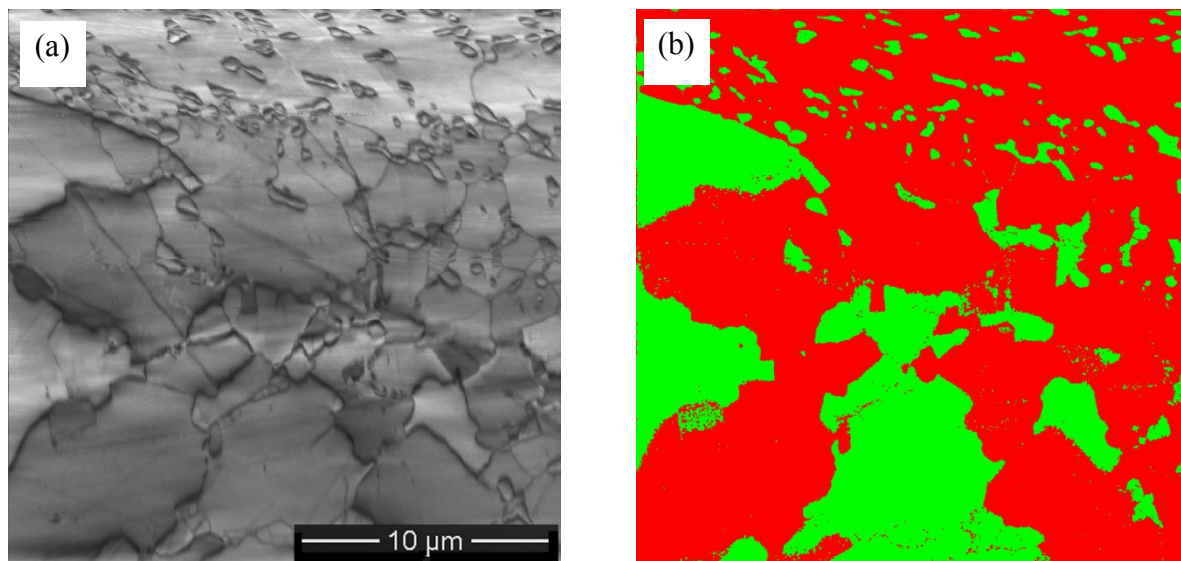


Figure 10. (a) SEM secondary electron image of the microstructure of an NbCrMo<sub>0.5</sub>Ta<sub>0.5</sub>TiZr alloy sample after compression at 1473 K and (b) respective phase map. The BCC phases are red and the FCC (Laves) phase is green.